

Sensitive room-temperature terahertz detection via the photothermoelectric effect in graphene

Xinghan Cai¹, Andrei B. Sushkov¹, Ryan J. Suess², Mohammad M. Jadidi², Gregory S. Jenkins¹, Luke O. Nyakiti³, Rachael L. Myers-Ward⁴, Shanshan Li², Jun Yan^{1,5}, D. Kurt Gaskill⁴, Thomas E. Murphy², H. Dennis Drew¹ and Michael S. Fuhrer^{1,6*}

Terahertz radiation has uses in applications ranging from security to medicine¹. However, sensitive room-temperature detection of terahertz radiation is notoriously difficult². The hot-electron photothermoelectric effect in graphene is a promising detection mechanism; photoexcited carriers rapidly thermalize due to strong electron–electron interactions^{3,4}, but lose energy to the lattice more slowly^{3,5}. The electron temperature gradient drives electron diffusion, and asymmetry due to local gating^{6,7} or dissimilar contact metals⁸ produces a net current via the thermoelectric effect. Here, we demonstrate a graphene thermoelectric terahertz photodetector with sensitivity exceeding 10 V W^{-1} (700 V W^{-1}) at room temperature and noise-equivalent power less than $1,100 \text{ pW Hz}^{-1/2}$ ($20 \text{ pW Hz}^{-1/2}$), referenced to the incident (absorbed) power. This implies a performance that is competitive with the best room-temperature terahertz detectors⁹ for an optimally coupled device, and time-resolved measurements indicate that our graphene detector is eight to nine orders of magnitude faster than those^{7,10}. A simple model of the response, including contact asymmetries (resistance, work function and Fermi-energy pinning) reproduces the qualitative features of the data, and indicates that orders-of-magnitude sensitivity improvements are possible.

Graphene has unique advantages for hot-electron photothermoelectric detection. Gapless graphene has strong interband absorption at all frequencies. The electronic heat capacity of single-layer graphene is much lower than in bulk materials, resulting in a larger change in temperature for the same absorbed energy. The photothermoelectric effect has a picosecond response time, set by the electron–phonon relaxation rate^{10,11}. Hot-electron effects have been exploited in graphene for sensitive bolometry in terahertz and millimetre-wave regimes at cryogenic temperatures by using temperature-dependent resistance in gapped bilayer graphene¹², which is sizable only at low temperature, or noise thermometry¹³, which requires complex radiofrequency electronics. In contrast, our photothermoelectric approach is temperature-insensitive and produces an observable d.c. signal, even under room-temperature conditions.

To realize our graphene hot-electron thermoelectric photodetector we generated an asymmetry by contacting graphene with dissimilar metals using a standard double-angle evaporation technique, as shown in Fig. 1a–e (see Methods). Figure 1f presents optical and atomic-force micrographs of the monolayer graphene device. Two metal electrodes, each consisting of partially overlapping Cr and Au regions, contact the monolayer graphene flake. The $3 \mu\text{m} \times 3 \mu\text{m}$ graphene channel is selected to be shorter than the estimated

electron diffusion length¹⁴. Figure 1g presents a schematic of our detector in cross-section. Figure 1h–k illustrates the principle of operation: electrons in graphene are heated by the incident light and the contacts serve as a heat sink, resulting in a non-uniform electron temperature $T(x)$ as a function of position x within the device (Fig. 1h). Because of the different metal contacts, the Fermi energy profile (Fig. 1i), and therefore the Seebeck coefficient (S ; Fig. 1j), are asymmetric across the device. Diffusion of hot electrons creates a potential gradient $\nabla V(x) = -S\nabla T(x)$ (Fig. 1k). The total signal is the integral of $\nabla V(x)$ over the device length (area under the curve in Fig. 1k) and is non-zero because of the asymmetry.

Figure 2 presents responsivity R , the ratio of the signal voltage to absorbed power, of the device to d.c. or a.c. Joule heating, near-infrared ($1.54 \mu\text{m}$) and terahertz ($119 \mu\text{m}$) excitation (see Methods). To better compare the response across such disparate wavelengths we define the responsivity using the absorbed power, rather than the incident power. Our device absorbs only a small fraction of the incident terahertz power (estimated from the measured sheet conductivity; see Methods and Supplementary Note 3); however, the absorption could in principle be increased by using multilayer graphene, using an antenna or tailoring a plasmonic resonance in graphene to match the incident frequency. Thus, results referenced to absorbed power highlight the ultimate potential for our device scheme. However, as we discuss in the following, even our unoptimized device with no antenna has performance referenced to the incident power that is unrivalled in its combination of speed and sensitivity. Figure 2a shows the two-probe conductance G as a function of gate voltage V_g measured from the point of minimum conductance $V_{g,\text{min}}$. The effective charge carrier mobility is $1,500 \text{ cm}^2 \text{ V}^{-1} \text{ s}^{-1}$, which is probably an underestimate of the true mobility due to inevitable contact resistance in the two-probe geometry. Figure 2b,c plots the responsivity $R(V_g)$ as a function of gate voltage for d.c. Joule heating and terahertz excitation, respectively. For both excitations, the peak responsivity appears at low carrier density, changes sign at $V_g - V_{g,\text{min}} = -20 \text{ V}$ and is small at large negative V_g . The overall shape and magnitude are comparable, suggesting that both signals are generated from the same mechanism—the hot-carrier thermoelectric effect. The terahertz responsivity is slightly larger than the d.c. responsivity, possibly reflecting a slight overestimation of the terahertz absorption due to (1) neglected contact resistance in estimating the conductivity of graphene or (2) inhomogeneity, which causes the average conductivity to be greater than the inverse of the average resistivity. At a later time (150 days), for the same device, we measured the conductance and responsivity to a.c.

¹Center for Nanophysics and Advanced Materials, University of Maryland, College Park, Maryland 20742-4111, USA, ²Institute for Research in Electronics and Applied Physics, University of Maryland, College Park, Maryland 20742, USA, ³Texas A&M University, Galveston, Texas 77553, USA, ⁴US Naval Research Laboratory, Washington DC 20375, USA, ⁵Department of Physics, University of Massachusetts, Amherst, Massachusetts 01003, USA, ⁶School of Physics, Monash University, 3800 Victoria, Australia. *e-mail: michael.fuhrer@monash.edu

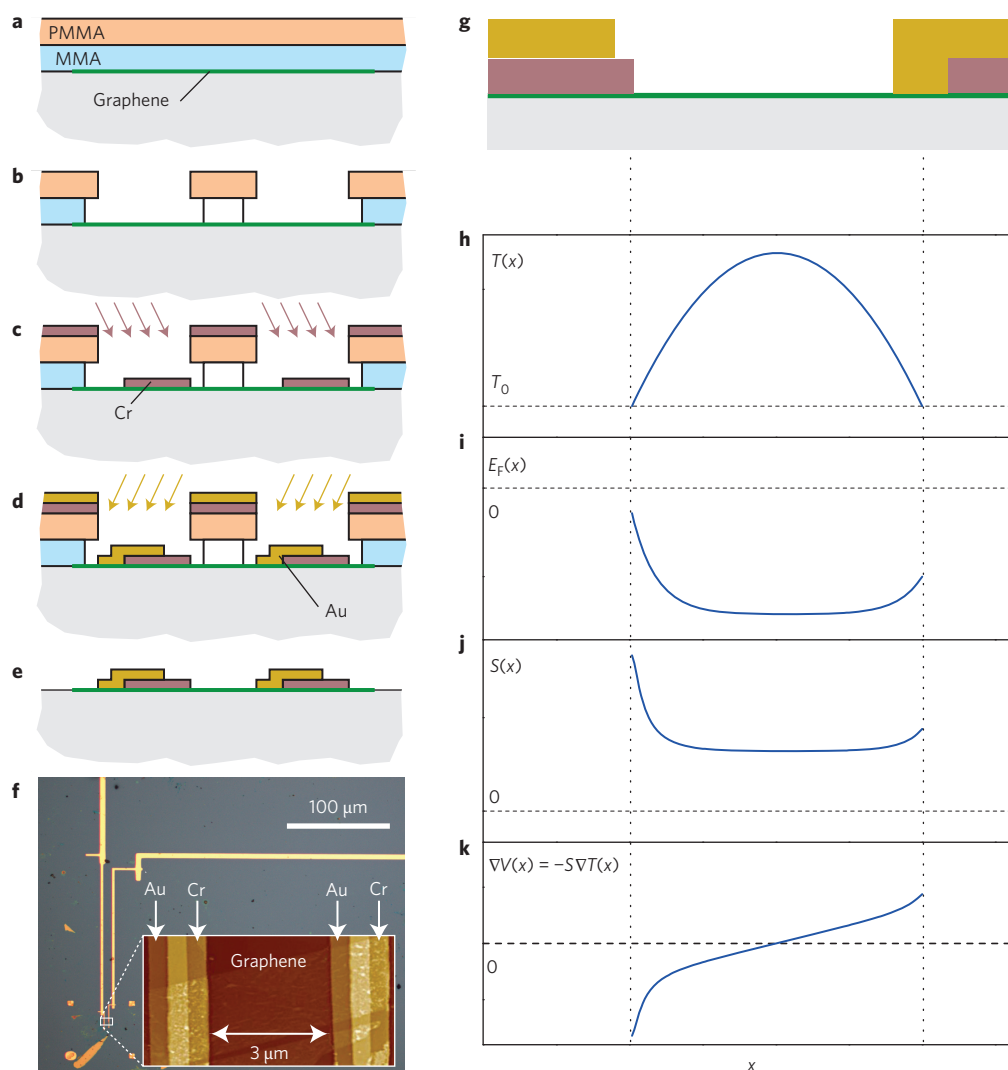


Figure 1 | Graphene photothermoelectric detector device fabrication and principle of operation. **a–e**, Lithographic sequence used to produce the graphene terahertz detector. A bilayer resist (MMA/PMMA; see Methods) is spun onto graphene on SiO_2/Si (**a**). Resist is patterned by an electron beam and developed (**b**). Successive angled evaporations of chromium (red arrows) (**c**) and gold (yellow arrows) (**d**), followed by liftoff, produce a single-layer graphene device with dissimilar metal contacts on opposing sides (shown schematically in **e**). **f**, Optical micrograph showing electrical contacts. Inset: Atomic force micrograph showing bimetallic contacts connected to an exfoliated graphene layer. **g**, Cross-sectional view of the device. **h–j**, Profiles across the device of electron temperature $T(x)$ (**h**), Fermi energy $E_F(x)$ (**i**), Seebeck coefficient $S(x)$ (**j**) and potential gradient $\nabla V(x) = -S\nabla T(x)$ (**k**). The photoresponse is the integral of $\nabla V(x)$ over the length of the device, or area under the curve in **k**.

Joule heating and near-infrared illumination (Fig. 2d–f). The device was degraded slightly, showing somewhat higher $V_{g,\text{min}}$ and slightly lower conductance. The responsivity under Joule heating (Fig. 2e) is also lower than previously measured (Fig. 2b), but has a similar functional form. The near-infrared responsivity is much lower than the far-infrared responsivity, possibly indicating the importance of optical phonon emission⁵ in hot-carrier relaxation for excitation energies exceeding the optical phonon energy (~ 160 meV). The near-infrared responsivity shows a different gate-voltage dependence, possibly due to the contribution of the photovoltaic effect^{6,15}. However, Fig. 2b,c,e,f shows that the thermoelectric signal persists from d.c. to near-infrared frequency with comparable responsivity, implying that the photothermoelectric effect is a promising mechanism for extraordinarily broadband detection of radiation.

Figure 3a shows the gate-voltage-dependent responsivity for a similar device, with a peak responsivity to terahertz excitation of 715 V W^{-1} . Figure 3b shows the measured gate voltage-dependent noise with no terahertz excitation (black line) and the calculated

Johnson–Nyquist noise floor $(4k_B T/G)^{1/2}$ (red line), where k_B is the Boltzmann constant and G is the measured conductance. The experimental noise only slightly exceeds the theoretical limit, indicating that nearly Johnson–Nyquist noise-limited performance is attainable. As shown in Fig. 3c, the noise-equivalent power (NEP) reaches a minimum level of $16 \text{ pW Hz}^{-1/2}$ at peak responsivity.

We now characterize the response time of our detectors. We first investigate the intrinsic time response of the devices using a pulse-coincidence technique^{7,10} with a $1.56 \mu\text{m}$ pulsed laser (see Methods). Figure 4a shows the photovoltage signal measured on another device (similar to the one shown in Fig. 1) due to a pump and probe beam as a function of the probe delay time τ_d at $T = 150 \text{ K}$. The dip of the signal at zero delay comes from nonlinearity in the photoresponse at low temperature^{7,10}. By fitting the data to a two-sided exponential decay (red line in Fig. 4a) we estimate an intrinsic response time of 10.5 ps due to electron–phonon relaxation. We also fabricated detectors using dissimilar metal electrodes to contact epitaxial single-layer graphene on (0001) semi-insulating

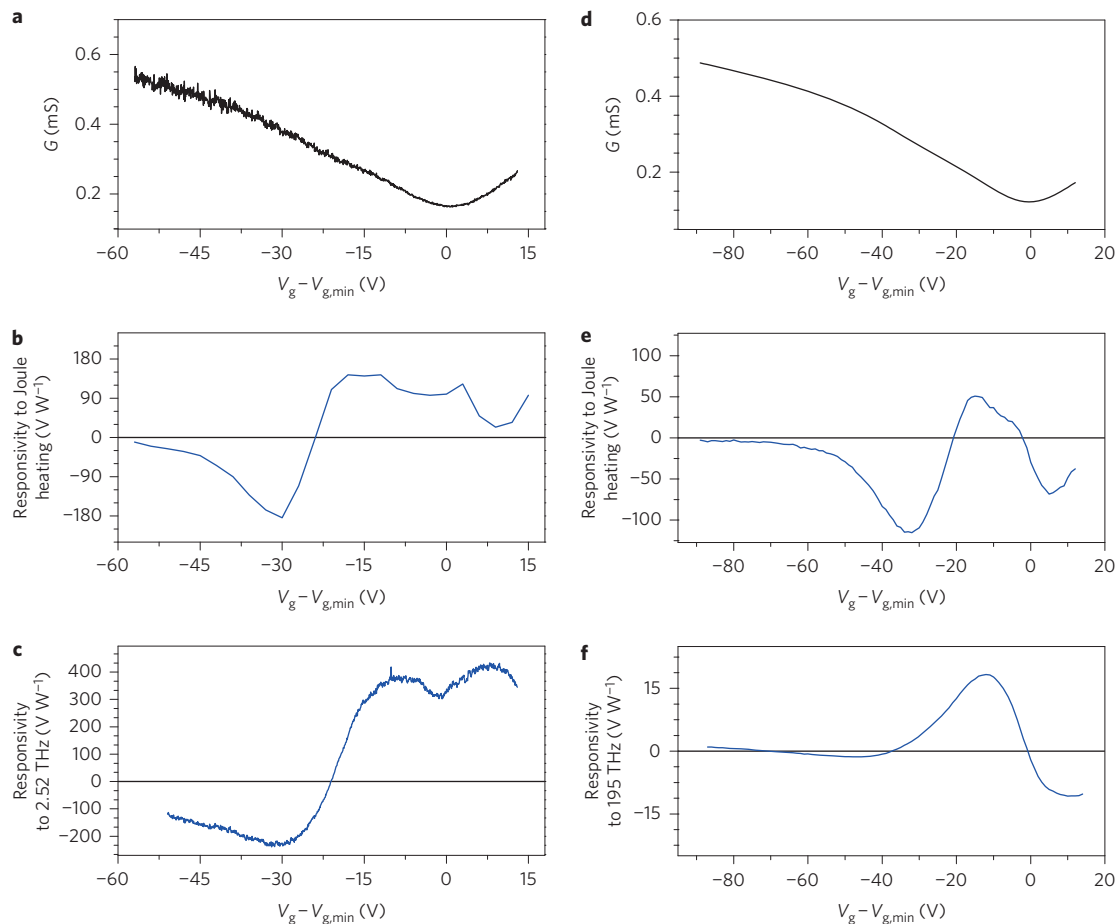


Figure 2 | Broadband thermoelectric responsivity of the graphene photothermoelectric detector. **a–f**, Electrical conductance (**a,d**), responsivity to Joule heating (**b,e**) and responsivity to radiation (**c,f**) as a function of gate voltage for the device shown in Fig. 1f at room temperature and in an ambient environment. Data in **d–f** were taken 150 days after data in **a–c**. In **a–c** the minimum conductivity point is $V_{g,\min} = 42$ V and in **d–f** it is $V_{g,\min} = 80$ V. Responsivity to Joule heating was measured at d.c. in **b** and at 15.7 Hz using the second harmonic technique in **e** (see Methods). In **c**, the responsivity to 119 μm wavelength terahertz radiation is shown referenced to the absorbed power, and **f** shows the response to 1.54 μm infrared radiation.

SiC (Fig. 4d, see Methods) and large-area chemical vapour deposition (CVD)-grown graphene on SiO_2/Si (Fig. 4e, see Methods), realizing devices capable of direct readout at microwave frequencies. Figure 4b shows the time-domain response of the epitaxial graphene device to ultrafast optical (800 nm wavelength) pulses at room temperature and Fig. 4c shows the response of the CVD graphene device to ultrafast terahertz (0–2 THz) pulses, recorded by a 40 GHz oscilloscope (see Methods). The active area of the CVD graphene device was $500 \mu\text{m} \times 500 \mu\text{m}$ (Fig. 4e) so as to collect more incident power, and the SiO_2/Si substrate enabled a gate-dependent photoresponse measurement. Figure 4c shows the differential response at $V_g = -40$ V subtracted from the response at $V_g = -20$ V and $V_g = 0$ V to eliminate any gate voltage-independent background. As shown in Fig. 4b, the full-width at half-maximum (FWHM) of the signal is 30 ps for 800 nm optical excitation. As the response is convolved with the 25 ps response of the oscilloscope itself, we conclude that the response time is significantly less than 30 ps, and consistent with the intrinsic 10.5 ps response time estimated in Fig. 4a. The electrical impulse response to terahertz excitation is 110 ps (Fig. 4c), which is slower because of the larger size (and capacitance) of the CVD device. Our results are consistent with other direct measurements of the thermal response time of graphene in the near-infrared^{11,16} and terahertz¹⁷, where the characteristic timescale was found to be 10–100 ps.

We now compare our device with existing technologies. The NEP of our device, $16 \text{ pW Hz}^{-1/2}$ referenced to the absorbed power, is

competitive with the best room-temperature low-frequency terahertz detectors⁹. However, a significant advantage of our device is its speed. Graphene-based room-temperature terahertz detectors based on a transistor geometry^{17–20} have shown sensitive detection at 358 GHz (ref. 19), but the responsivity of our device and NEP referenced to incident power are still superior to these devices. We anticipate room for a two orders-of-magnitude sensitivity improvement by increasing the absorption through, for example, antenna coupling, and further orders-of-magnitude improvements from increasing the thermopower asymmetry, as discussed in the following. For frequencies above 1 THz, our reported responsivity is five to six orders of magnitude larger than in earlier graphene-based detectors^{17,20}, in part because photothermoelectric detection does not suffer from the high-frequency roll-off that is characteristic of field-effect transistor (FET)-based detectors. Beyond graphene, there are few existing terahertz detector technologies with sub-100 ps response times. Schottky diodes can detect 100 ps signal modulations²¹, but their responsivity decreases rapidly ($1/f^2$) with frequency f , and measured NEP values are $0.3\text{--}10 \text{ nW Hz}^{-1/2}$ at 1 THz, increasing rapidly above 1 THz. An intraband superlattice detector²² has achieved a response time of 20 ps, but the responsivity was $50 \mu\text{A W}^{-1}$ (2.5 mV W^{-1} , assuming 50Ω load) at 6 THz, and a nanosized FET²³ demonstrated a 30 ps response at 5 THz with an estimated NEP of $>10 \mu\text{W Hz}^{-1/2}$. We therefore believe our detector uniquely offers fast, sensitive detection in the few-terahertz regime, with orders-of-magnitude improvement in

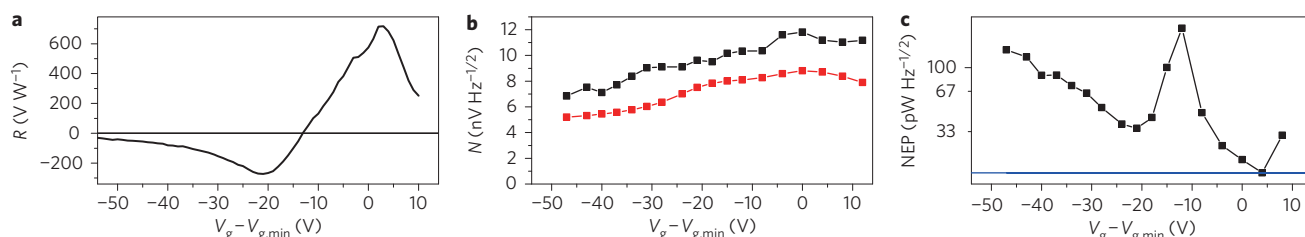


Figure 3 | Noise-equivalent power of the graphene photothermoelectric detector. **a–c**, Responsivity to 119 μm wavelength terahertz radiation (**a**), measured noise (black line) and calculated Johnson-Nyquist noise (red line; **b**), and measured noise-equivalent power (NEP; **c**) as a function of gate voltage for a device similar to the one shown in Fig. 1f. The blue line corresponds to NEP = 16 $\text{pW Hz}^{-1/2}$. Responsivity and NEP are referenced to the absorbed power. For clarity, NEP is plotted on a log scale.

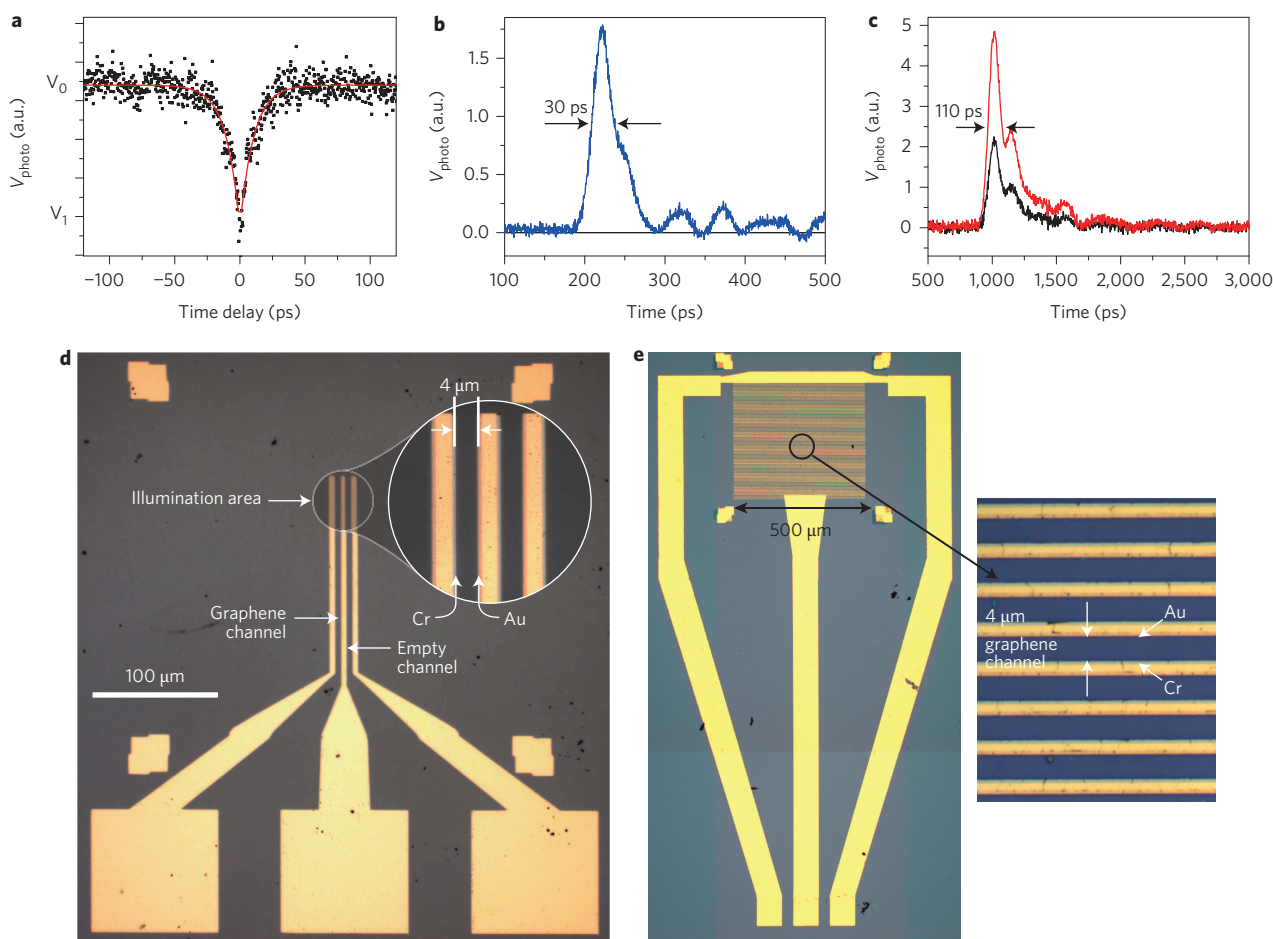


Figure 4 | Response time of the graphene photothermoelectric detector. **a**, Photoresponse from pump-probe laser pulses as a function of delay time at 150 K. Red solid line shows a best fit assuming exponential decay of hot-electron temperature. **b**, Time-domain photoresponse to pulsed laser excitation at 800 nm wavelength recorded by a 40 GHz sampling oscilloscope for a device fabricated on SiC (see Methods). The full-width at half-maximum (FWHM) response is ~ 30 ps. **c**, Time-domain photoresponse to pulsed laser excitation in the terahertz range recorded by a 40 GHz sampling oscilloscope for a chemical vapour deposition-grown graphene device (see Methods). The FWHM response is ~ 110 ps. Black (red) line shows the response at $V_g = -20$ V (0 V). **d, e**, Micrographs of the devices for the measurements in **b** and **c**, respectively.

responsivity and NEP compared to existing terahertz detectors with sub-100 ps response times.

We now estimate the magnitude of the thermoelectric responsivity R , theoretically. First, we ignore electron-acoustic phonon coupling^{14,24}, and make a simple estimate based on diffusive cooling by the electrodes. According to the Wiedemann-Franz law and Mott relation^{25,26}, the electron thermal conductivity of graphene is $\kappa = L\sigma T$ and the Seebeck coefficient is $S = LT(d\ln\sigma/dE_F)$, where σ is the conductivity and the Lorentz number $L = \pi^2 k_B^2/3e^2$. A

thermal difference ΔT results in a voltage $V = -S\Delta T$ and heat flux $Q = \kappa\Delta T$. Then, $R = |V/Q| = (1/\sigma E_F)(d\ln\sigma/d\ln E_F) \approx 2/\sigma E_F$. The responsivity is maximized at small E_F and small σ . These quantities are limited by disorder; for graphene on SiO₂ the minimal values are roughly $\sigma = 0.2$ mS and $E_F = 50$ meV (ref. 27), giving a maximum responsivity of 2×10^5 V W^{-1} , which is almost three orders of magnitude larger than our experimental result.

We next model the response of our device considering three sources of asymmetry and qualitatively obtain their influence on

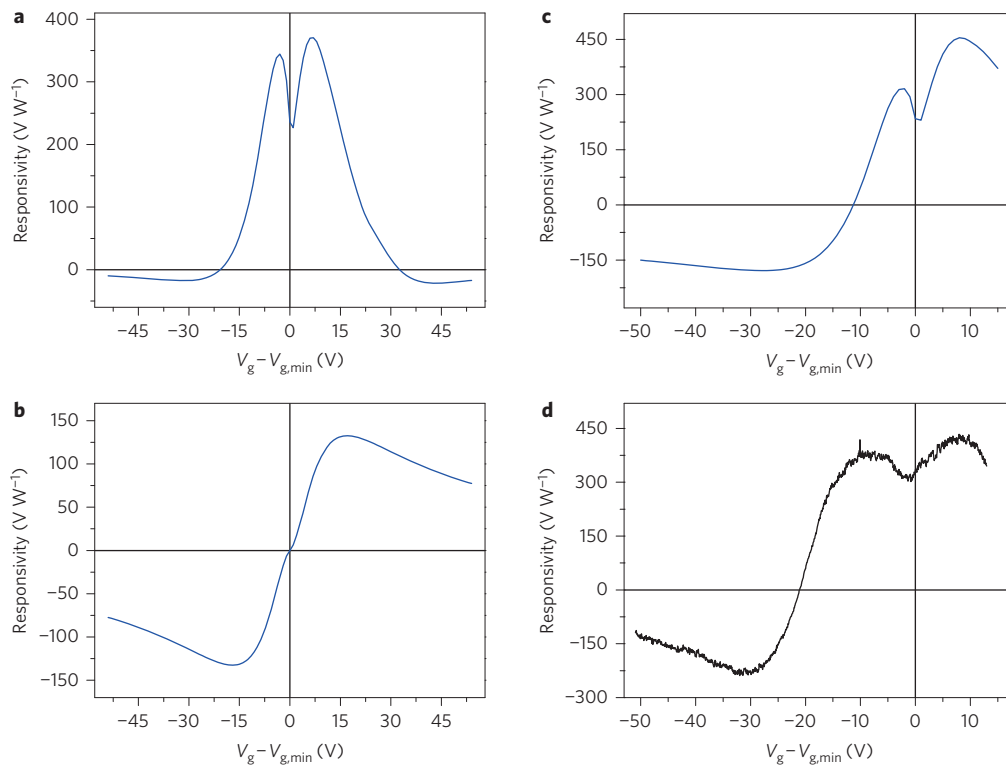


Figure 5 | Simulated responsivity of the graphene photothermoelectric detector. **a–c**, The modelled responsivity of the device as induced by the work function difference of Cr and Au and different chemical potential pinning near both contacts (**a**), purely induced by an additional contact resistance near the Au electrode (**b**), and induced by the asymmetries shown in **a** and **b** together (**c**). **d**, Measured responsivity of our device to 119 μm wavelength terahertz radiation (replotted from Fig. 2c).

the thermoelectric signal. We consider two effects in the models: (1) asymmetry due to the contact metals, including pinning of the chemical potential at the graphene/metal interface and the long-ranged electrostatic effect of the nearby metal on graphene due to their different work functions²⁸ and (2) asymmetry in the contact resistance²⁹. The first effect is inevitable in our dissimilar-metal-contacted devices. Additional scattering in graphene caused by metal near the contact may contribute to additional contact resistance²⁹ and it is reasonable to suppose that this effect may be asymmetric for different contact metals. See Supplementary Note 4 for details of the models.

Figure 5 summarizes the results of the modelling, where we have used realistic parameters for gold and chromium metals in modelling the contact chemical potential pinning and work function²⁸ and an additional contact resistance of $R_c = 33.5 \Omega$ for the gold electrode. In general, we find that asymmetry in the contact metal produces a signal symmetric in $|V_g - V_{g,\text{min}}|$ (Fig. 5a), while additional contact resistance produces a signal antisymmetric in $|V_g - V_{g,\text{min}}|$ (Fig. 5b). The combined effect of contact metal and contact resistance asymmetry (Fig. 5c) describes well the magnitude and shape of the gate-voltage-dependent response to terahertz excitation in the real device (replotted in Fig. 5d). We can identify the overall asymmetry as arising from contact resistance, and the dip in responsivity near charge neutrality as being due to contact work function/Fermi-energy pinning effects. The model has several adjustable parameters (see Methods), and verification will require more work to systematically vary these and observe their effect on responsivity. However, the fact that we can model the data with physically reasonable parameters indicates that the model captures the essential operating principles of the device. We note that the responsivity is several orders of magnitude smaller than the maximum thermopower that might be expected for local heating

of a p–n junction. This suggests that significant improvements of room-temperature graphene terahertz detectors are possible using local gates or locally doped regions to define p–n junctions.

Methods

Single-layer graphene was exfoliated from bulk graphite onto a substrate of 300 nm SiO_2 over low-doped Si (100–250 Ωcm). Supplementary Fig. 1 shows a Raman spectrum of the graphene used in the device in Fig. 1f. Dissimilar metal contacts were fabricated in one lithographic step using a tilted-angle shadow evaporation technique. The evaporation mask was fabricated using a standard electron-beam lithography technique using a bilayer resist (methyl methacrylate (8.5%)/methacrylic acid copolymer (MMA) and poly(methyl methacrylate) (PMMA), both Micro Chem Corp.)³⁰. Layers of chromium (20 nm) and gold (20 nm) were deposited at different evaporating angles.

The d.c. thermoelectric responsivity was characterized by applying a d.c. voltage across the electrodes and measuring the resulting current $I_1 = I + I_{\text{thermal}}$ and $I_2 = -I + I_{\text{thermal}}$ under both polarities of the applied voltage $\pm V$, where I is the current generated by the bias voltage and I_{thermal} is the thermoelectric current. The applied voltage was 0.2 V and the Joule heating power was tens of microwatts. The thermoelectric responsivity was then $R = V_{\text{thermal}}/P = I_{\text{thermal}}/I^2 = 2(I_1 + I_2)/(I_1 - I_2)^2$. We verified that I_{thermal} was much less than I in the measurement. Similarly, for low-frequency a.c. excitation, a bias current $I_{\text{ac}}(t) = I_0 \sin(\omega t)$ at frequency $\omega = 15.7 \text{ Hz}$ was applied to the device. Measurements were made in the regime where the thermoelectric voltage was much smaller than V_0 , the amplitude of the applied voltage. The observed thermoelectric voltage $V(t)$ was proportional to the absorbed power, $P(t) = (GV_0^2/2)[1 - \cos(2\omega t)]$, where G is conductance. This second harmonic component of the voltage $V_{2\omega} \cos(2\omega t)$ was detected by a lock-in amplifier, giving the responsivity $R = 2GV_{2\omega}/(I_0^2)$. For optical excitation we uniformly illuminated the device with a chopped continuous-wave laser and detected the open-circuit photovoltage signal by using a voltage preamplifier and lock-in amplifier. The wavelength was 1.54 μm for the near-infrared laser and 119 μm for the terahertz laser generated by CO_2 -laser-pumped methanol gas. We measured five devices and all showed a similar gate-dependent photoreponse. To calculate the absorbed power under far-infrared excitation, we performed scanning photovoltage measurements to characterize the beam profile and determine the incident power intensity on the graphene area (Supplementary Fig. 3). We treated the device as a conducting layer sandwiched by air and a silicon substrate to find the real electric field at the graphene

layer and considered Drude absorption to estimate the quantum efficiency (Supplementary Note 3). All the measurements mentioned above were performed under ambient conditions at room temperature. For the noise measurement in Fig. 3b, the gate voltage-dependent noise was measured with a lock-in amplifier at frequency $f = 331$ Hz, the same frequency used to chop the terahertz laser for the responsivity measurement in Fig. 3a.

The intrinsic speed of our graphene photothermoelectric detectors was measured using the asynchronous optical sampling (ASOPS) method³¹ with an ultrafast pulsed laser with a wavelength of 1.56 μm , pulse width of ~ 60 fs and average power of 50 mW as pump and probe sources, with a maximum scan length of 10 ns and scan resolution of ~ 100 fs. The sample was mounted in an optical cryostat at 150 K. The photovoltage was measured as a function of the pump-probe delay time. We also prepared devices suitable for direct time-domain measurement of their extrinsic response time using the same tilted-angle shadow evaporation technique. For optical (800 nm) excitation the starting material was single-layer epitaxial graphene on (0001) semi-insulating (resistivity $> 1 \times 10^9 \Omega \text{ cm}$) SiC (see ref. 32 for additional details). The semi-insulating SiC substrate eliminated the stray capacitance of device to substrate and absorption of the incident light by the substrate. The graphene channel was 4 μm long and 100 μm wide, as shown in Fig. 4d. The pads were contacted by a three-tip radiofrequency ground-signal-ground probe. The photoresponse was excited by a pulsed laser beam with a wavelength of 800 nm, pulse width of ~ 50 fs, repetition rate of 1 kHz and pulse energy of 250 nJ. The device for terahertz excitation was fabricated using CVD-grown single-layer graphene on a substrate of 300 nm SiO₂ over low-doped Si (100–250 $\Omega \text{ cm}$). As shown in Fig. 4e, many graphene channels were connected in series to enhance the signal. Each graphene channel was 4 μm long and 500 μm wide. Broadband terahertz pulses with a duration of ~ 1 ps and a spectrum spanning 0–2 THz were produced through optical rectification of femtosecond pulses in a lithium niobate prism³³, and focused onto the device through a polymethylpentene (TPX) lens. The focused terahertz pulses had a beam diameter of ~ 1 mm and a pulse energy of 160 nJ at a repetition rate of 1 kHz. The output signal was recorded using a high-speed (bandwidth = 40 GHz) sampling oscilloscope.

Received 9 February 2014; accepted 30 July 2014;
published online 7 September 2014

References

1. Tonouchi, M. Cutting-edge terahertz technology. *Nature Photon.* **1**, 97–105 (2007).
2. Chan, W. L., Deibel, J. & Mittleman, D. M. Imaging with terahertz radiation. *Rep. Prog. Phys.* **70**, 1325–1379 (2007).
3. Breusing, M., Ropers, C. & Elsaesser, T. Ultrafast carrier dynamics in graphite. *Phys. Rev. Lett.* **102**, 086809 (2009).
4. Tse, W.-K., Hwang, E. H. & Das Sarma, S. Ballistic hot electron transport in graphene. *Appl. Phys. Lett.* **93**, 023128 (2008).
5. Lui, C. H., Mak, K. F., Shan, J. & Heinz, T. F. Ultrafast photoluminescence from graphene. *Phys. Rev. Lett.* **105**, 127404 (2010).
6. Gabor, N. M. *et al.* Hot carrier-assisted intrinsic photoresponse in graphene. *Science* **334**, 648–652 (2011).
7. Graham, M. W., Shi, S.-F., Ralph, D. C., Park, J. & McEuen, P. L. Photocurrent measurement of supercollision cooling in graphene. *Nature Phys.* **9**, 103–108 (2013).
8. Xia, F. *et al.* Photocurrent imaging and efficient photon detection in a graphene transistor. *Nano Lett.* **9**, 1039–1044 (2009).
9. Sizov, F. & Rogalski, A. THz detectors. *Prog. Quant. Electron.* **34**, 278–347 (2010).
10. Kim, M.-H. *et al.* Photothermal response in dual-gated bilayer graphene. *Phys. Rev. Lett.* **110**, 247402 (2013).
11. Mueller, T., Xia, F. & Avouris, P. Graphene photodetectors for high-speed optical communications. *Nature Photon.* **4**, 297–301 (2010).
12. Yan, J. *et al.* Dual-gated bilayer graphene hot-electron bolometer. *Nature Nanotech.* **7**, 472–478 (2012).
13. Fong, K. C. & Schwab, K. C. Ultrasensitive and wide-bandwidth thermal measurement of graphene at low temperatures. *Phys. Rev. X* **2**, 031006 (2012).
14. Song, J. C. W., Rudner, M. S., Marcus, C. M. & Levitov, L. S. Hot carrier transport and photocurrent response in graphene. *Nano Lett.* **11**, 4688–4692 (2011).
15. Park, J., Ahn, Y. H. & Ruiz-Vargas, C. Imaging of photocurrent generation and collection in single-layer graphene. *Nano Lett.* **9**, 1742–1746 (2009).
16. Pospishil, A. *et al.* CMOS-compatible graphene photodetector covering all optical communication bands. *Nature Photon.* **7**, 892–896 (2013).
17. Mittendorff, M. *et al.* Ultrafast graphene-based broadband THz detector. *Appl. Phys. Lett.* **103**, 021113 (2013).
18. Vicarelli, L. *et al.* Graphene field-effect transistors as room-temperature terahertz detectors. *Nature Mater.* **11**, 865–871 (2012).
19. Spirito, D. *et al.* High performance bilayer-graphene terahertz detectors. *Appl. Phys. Lett.* **104**, 061111 (2014).
20. Muraviev, A. V. *et al.* Plasmonic and bolometric terahertz detection by graphene field-effect transistor. *Appl. Phys. Lett.* **103**, 181114 (2013).
21. Bozhkov, V. G. Semiconductor detectors, mixers, and frequency multipliers for the terahertz band. *Radiophys. Quantum Electron.* **46**, 631–656 (2003).
22. Klappenberger, F. *et al.* Broadband semiconductor superlattice detector for THz radiation. *Appl. Phys. Lett.* **78**, 1673–1675 (2001).
23. Preu, S. *et al.* Ultra-fast transistor-based detectors for precise timing of near infrared and THz signals. *Opt. Express* **21**, 17941–17950 (2013).
24. Viljas, J. K. & Heikkilä, T. T. Electron-phonon heat transfer in monolayer and bilayer graphene. *Phys. Rev. B* **81**, 245404 (2010).
25. Zuev, Y. M., Chang, W. & Kim, P. Thermoelectric and magnetothermoelectric transport measurements of graphene. *Phys. Rev. Lett.* **102**, 096807 (2009).
26. Wei, P., Bao, W., Pu, Y., Lau, C. N. & Shi, J. Anomalous thermoelectric transport of Dirac particles in graphene. *Phys. Rev. Lett.* **102**, 166808 (2009).
27. Adam, S., Hwang, E. H., Galitski, V. M. & Das Sarma, S. A self-consistent theory for graphene transport. *Proc. Natl Acad. Sci. USA* **104**, 18392–18397 (2007).
28. Khomyakov, P. A., Starikov, A. A., Brocks, G. & Kelly, P. J. Nonlinear screening of charges induced in graphene by metal contacts. *Phys. Rev. B* **82**, 115437 (2010).
29. Huard, B., Stander, N., Sulpizio, J. A. & Goldhaber-Gordon, D. Evidence of the role of contacts on the observed electron-hole asymmetry in graphene. *Phys. Rev. B* **78**, 121402(R) (2008).
30. Niemeyer, J. & Kose, V. Observation of large dc supercurrents at nonzero voltages in Josephson tunnel junctions. *Appl. Phys. Lett.* **29**, 380–382 (1976).
31. Bartels, A. *et al.* Ultrafast time-domain spectroscopy based on high-speed asynchronous optical sampling. *Rev. Sci. Instrum.* **78**, 035107 (2007).
32. Nyakiti, L. O. *et al.* Enabling graphene-based technologies: toward wafer-scale production of epitaxial graphene. *Mater. Res. Soc. Bull.* **37**, 1149–1157 (2012).
33. Hebling, J., Yeh, K.-L., Hoffmann, M. C., Bartal, B. & Nelson, K. A. Generation of high-power terahertz pulses by tilted-pulse-front excitation and their application possibilities. *J. Opt. Soc. Am. B* **25**, B6 (2008).

Acknowledgements

This work was sponsored by the US Office of Naval Research (awards nos. N000140911064, N000141310712 and N000141310865), the National Science Foundation (ECCS 1309750) and Intelligence Advanced Research Projects Activity. M.S.F. was supported in part by an Australian Research Council Laureate Fellowship. The authors thank V. D. Wheeler and C. Eddy, Jr, for discussions.

Author contributions

X.C., A.B.S., J.Y., T.E.M., H.D.D. and M.S.F. conceived the experiments. X.C. fabricated the graphene photodetectors. X.C., A.B.S. and G.S.J. carried out the terahertz measurements. X.C., R.J.S., M.M.J. and S.L. carried out the near-infrared and pulsed laser measurements. X.C. and J.Y. carried out the d.c. and a.c. transport measurements. L.O.N., R.L.M.-W. and D.K.G. synthesized the graphene on SiC. All authors contributed to writing the manuscript.

Additional information

Supplementary information is available in the [online version](#) of the paper. Reprints and permissions information is available online at www.nature.com/reprints. Correspondence and requests for materials should be addressed to M.S.F.

Competing financial interests

The authors declare no competing financial interests.